

**Optical pulling using topologically protected one way transport surface-arc waves**Neng Wang <sup>1</sup>, Ruo-Yang Zhang,<sup>2,\*</sup> Qinghua Guo,<sup>2</sup> Shubo Wang <sup>3</sup>, Guo Ping Wang,<sup>1</sup> and C. T. Chan<sup>2</sup><sup>1</sup>*Institute of Microscale Optoelectronics, Shenzhen University, Shenzhen 518060, China*<sup>2</sup>*Department of Physics, The Hong Kong University of Science and Technology, Clear Water Bay, Hong Kong, China*<sup>3</sup>*Department of Physics, City University of Hong Kong, Hong Kong, China*

(Received 17 August 2020; revised 2 January 2022; accepted 5 January 2022; published 13 January 2022)

Optical pulling is a counterintuitive phenomenon whereby light can pull particles against its propagation direction, but usually it is necessary to optimize both the incident beam and the manipulated particles. Here, we propose a robust optical pulling scheme using an air waveguide sandwiched between two chiral hyperbolic metamaterials carrying Weyl points. The pulling force is induced by mode conversion between two topologically protected chiral surface arcs supported on the two metamaterial surfaces of the waveguide. We prove that the optical pulling force is totally attributed to the Minkowski-type momentum of light and proportional to the wave-number difference between the two surface-arc waves, thus the pulling force is robust against the material, shape, and size of the particle. Thanks to the backscattering immunity of the surface-arc waves and the in-plane isotropy of the metamaterials, robust optical pulling can be achieved even in a curved waveguide, going beyond standard mechanisms of straight-line pulling.

DOI: [10.1103/PhysRevB.105.014104](https://doi.org/10.1103/PhysRevB.105.014104)**I. INTRODUCTION**

Optical pulling [1–11], which is the counterintuitive idea of using light to pull a particle towards the source, has attracted a great deal of attention recently. Optical pulling forces arise when the incident light transfers a backward linear momentum to the particle via light-matter interaction, which requires the forward scattering to be enhanced and the backward scattering to be suppressed [2–4]. In free space, optical pulling can be achieved by using structured light beams such as a Bessel beam [3–5] or the interference of multiple beams [7]. The technical difficulty in realizing long-range structured beams limits the application of optical pulling [8]. Furthermore, to achieve enhanced forward scattering, multipoles must be simultaneously excited, which renders the optical pulling material- and size-dependent [3,6,11]. These problems can be partially solved by changing the background from free space to a waveguide [12–20] or metamaterials [21,22], such as using the guided waves supported in a double-mode photonic crystal waveguide [17–19]. However, due to the restriction of reciprocity, the material and the shape of the particle have to be carefully optimized in order to suppress the backward scattering.

Using topologically protected one way transport surface waves instead of topologically trivial guided waves can enhance the efficacy of optical pulling, since the backscattering of surface waves is completely suppressed for a particle with an arbitrary shape and size and of arbitrary material [23–35]. Wang *et al.* first proposed using the chiral surface wave supported in two-dimensional (2D) magneto-optical photonic crystals to realize robust optical pulling [36].

However, the practical operating frequency range (gigahertz) of magneto-optical materials rarely overlaps with that of optical manipulation (greater than terahertz), making the optical force negligibly small compared to other forces. In addition, the spatial inhomogeneity of field intensity due to lattice structures can result in local equilibria which work against sustainable optical pulling.

In three-dimensional (3D) topological systems possessing Weyl nodes, the topological charges of Weyl points ensure the existence of chiral surface bands whose equifrequency sections form “Fermi arcs” (alternatively called surface arcs for general kinds of waves) that bridge the disconnected equifrequency surfaces (EFSs) of bulk states [37–57]. Such chiral surface arcs can exist in inversion-symmetry-broken systems while preserving time-reversal symmetry (TRS) [37,38]. Thanks to the relatively low technological threshold to break inversion symmetry in photonic systems, the surface-arc states have been observed experimentally in regimes ranging from microwave [38,52,53] to near-infrared [55], and novel functional transport effects using surface-arc waves have been realized, such as surface negative refraction [56] and surface-arc-assisted resonant transmission [57]. In addition to photonic crystals [38,50,51,53], Weyl points and chiral surface arcs can emerge in homogenized metamaterials in the long-wavelength limit, e.g., chiral hyperbolic metamaterials (CHMs) [37,38,50].

In this paper, we propose a method to realize robust long-range optical pulling by using two surface-arc modes in a planar air waveguide sandwiched by two CHMs with topologically charged EFSs. Unlike in 2D magneto-optical photonic crystals [36], the well-designed 3D CHMs respecting TRS can operate at high frequencies to induce a considerable optical force. The linear momentum of a surface wave on a homogeneous medium can be directly determined by the wave

\*Corresponding author: ruoyangzhang@ust.hk

vector [58,59], in contrast to the ambiguous relation between the linear momentum of a Bloch state and its Bloch wave vector in periodic systems [20,36], and hence the mechanism of momentum transfer is much clearer in our system than in photonic crystals. Based on a rigorous derivation, we obtained the closed-form expression for the longitudinal (along the surface wave propagating direction) optical force on a particle inside the waveguide, which reveals that the longitudinal optical force is totally converted from the Minkowski-type momentum of light, and proportional to the wave-number difference of the incident and scattered surface-arc states. Therefore, once we select the surface-arc state with the relatively smaller wave number as the incident one, the particle is always subjected to a pulling force towards the source irrespective of its size, shape, and material. Due to the homogeneity of the CHMs in the long-wavelength-limit, the field intensity distribution of the surface-arc wave is uniform along the propagating direction, which avoids the local equilibria induced by the intensity gradient force, thereby enabling consistent pulling of the particle toward the source. Moreover, the CHMs are isotropic in the  $xy$  plane, and the chiral surface arcs on any truncated surface parallel to the  $z$  axis have the same dispersion, making the surface waves travel around arbitrary corners without any refraction. Thus, a particle can be pulled continuously in a curved waveguide.

## II. BULK AND SURFACE-ARC DISPERSION OF THE CHM

A generic class of homogenized CHMs can be described by a Drude-Lorentz model with chiral magnetoelectric coupling [38,49,51,55]. Here, we assume that the metamaterials have a Drude-like dispersion in the  $z$  direction, and isotropic Lorentz resonances in the  $xy$  subspace. Additionally, the aligned electric and magnetic dipoles are chirally coupled in the  $xy$  plane. From the microscopic model by ignoring damping for simplicity (see the Supplemental Material [60], Sec. 1), we arrive at a macroscopic effective medium depicted by the constitutive relation  $\mathbf{D} = \epsilon_0 \vec{\epsilon}(\omega) \mathbf{E} + \frac{i}{c} \vec{\kappa}(\omega) \mathbf{H}$ ,  $\mathbf{B} = \mu_0 \vec{\mu}(\omega) \mathbf{H} - \frac{i}{c} \vec{\kappa}^T(\omega) \mathbf{E}$ , and the constitutive tensors

$$\begin{aligned} \vec{\epsilon}(\omega) &= \left( \epsilon_\infty + \frac{\alpha \omega_0^2}{\omega_0^2 - \omega^2} \right) \vec{I}_{xy} + \left( 1 - \frac{\omega_p^2}{\omega^2} \right) \hat{z}\hat{z}, \\ \vec{\mu}(\omega) &= \left( 1 + \frac{\beta \omega^2}{\omega_0^2 - \omega^2} \right) \vec{I}_{xy} + \hat{z}\hat{z}, \\ \vec{\kappa}(\omega) &= \kappa(\omega) \vec{I}_{xy} = \pm \frac{\sqrt{\alpha\beta} \omega_0 \omega}{\omega_0^2 - \omega^2} \vec{I}_{xy}, \end{aligned} \quad (1)$$

where  $\omega$  is the angular frequency,  $\omega_0, \omega_p$  are the Lorentz resonance and plasma frequencies, respectively,  $\epsilon_\infty$  denotes the asymptotic relative permittivity in the  $xy$  plane as  $\omega \rightarrow \infty$ , and  $\alpha, \beta$  are two positive parameters characterizing the strengths of Lorentz oscillation and chiral coupling. Since Eq. (1) is deduced from the microscopic Hermitian dynamics (see the Supplemental Material, Sec. 1), the eigenfrequency  $\omega(\mathbf{k})$  is ensured to be real, where  $\mathbf{k}$  is the plane-wave vector of an eigenmode. The band structure is plotted in Fig. 1(a). As the chiral coupling breaks inversion symmetry while it preserves TRS, two pairs of Weyl points emerge symmetrically

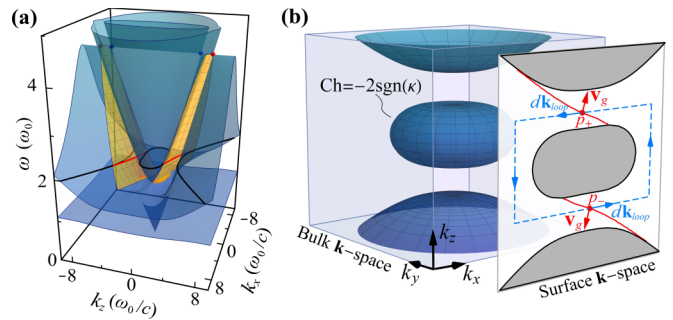


FIG. 1. (a) Band structure of the CHM given by Eq. (1) with the parameters  $\omega_p = 2\sqrt{5}\omega_0$ ,  $\alpha = 1.2$ ,  $\beta = 0.375$ , where four Weyl points with the same charge  $\text{sgn}(\kappa)$  (red nodes) and  $\text{sgn}(\kappa)$  (blue nodes) are located at the plasma frequency  $\omega_p$ . The yellow sheets denote the bands of chiral surface states on the interface between the metamaterial and air with the surface normal  $\hat{n} = -\hat{y}$ . (b) Bulk EFSs at  $\omega = 2\omega_0$  [corresponding to the black section line in (a)], comprised of a spheroid with  $\text{Ch} = -2\text{sgn}(\kappa)$  and two hyperbolic sheets. Two surface arcs (red lines) bridge disjoint projected bulk EFSs, intersecting a rectangular loop (blue dashed line) at  $p_\pm$ . Counting the chirality  $\chi = \text{sgn}(\mathbf{v}_g \cdot d\mathbf{k}_{\text{loop}})$  at each intersection, the summation equals the Chern number of the EFS enclosed by the loop.

on the line of  $k_x = k_y = 0$  at the plasma frequency  $\omega_p$ . If the frequency is in-between  $\max\{\omega_0/\sqrt{1+\alpha/\epsilon_\infty}, \omega_0/\sqrt{1-\beta}\}$  and  $\omega_p$ , Eq. (1) gives a type-I hyperbolic medium ( $\epsilon_{xx} = \epsilon_{yy} > 0, \epsilon_{zz} < 0, \mu_{xx} = \mu_{yy} > 0$ ) [61] with chiral coupling  $\vec{\kappa}$ . Its bulk EFSs consist of a closed spheroid and a hyperboloid of two sheets, separated by two complete  $k_z$ -momentum gaps. The spheroidal EFS and each hyperbolic sheet carry topological charges (i.e., Chern numbers)  $\text{Ch} = -2\text{sgn}(\kappa)$  and  $\text{Ch} = \text{sgn}(\kappa)$ , respectively [37]. In the Supplemental Material [60], Sec. 2, we showed that such CHMs can be realized using metallic helical structures.

When the metamaterial is in contact with air at a flat surface parallel to the  $z$  axis, the nontrivial Chern numbers of the EFSs indicate the existence of surface states confined on that surface which disperse as open arcs bridging the projected EFSs [37], according to the correspondence between bulk EFSs and surface arcs [44,45]. As shown in Fig. 1(b), since the spheroidal EFS has  $\text{Ch} = -2\text{sgn}(\kappa)$ , two surface arcs tangentially attaching to the bulk EFS stretch across the  $k_z$  gaps and connect with the upper and lower charge-1 hyperbolic sheets, respectively. The gapless surface arcs at different frequencies sweep out two surface bands (colored in yellow) filling the bulk band gaps, as shown in Fig. 1(a). Consider a virtual equifrequency loop enclosing the projected spheroidal EFS and inevitably intersecting with the two surface arcs, where the orientation of the loop is counterclockwise viewed from the top of the truncated surface. At an intersection point  $p$ , we define the chirality of the surface arc as  $\chi_p = \text{sgn}[d\mathbf{k}_{\text{loop}} \cdot \mathbf{v}_g]$  [45], where  $d\mathbf{k}_{\text{loop}}$  is the positive tangent vector of the loop, and  $\mathbf{v}_g$ , normal to the surface arc, denotes the group velocity of the surface state at  $p$ . The summation of the chirality of all intersections equals the Chern number of the EFS enclosed by the loop, namely  $\sum_p \chi_p = \text{Ch} = -2\text{sgn}(\kappa)$ . For a rectangular loop in Fig. 1(b), the two horizontal paths along  $k_z = \pm k_{z0}$  intersect with the two surface arcs at  $p_+, p_-$

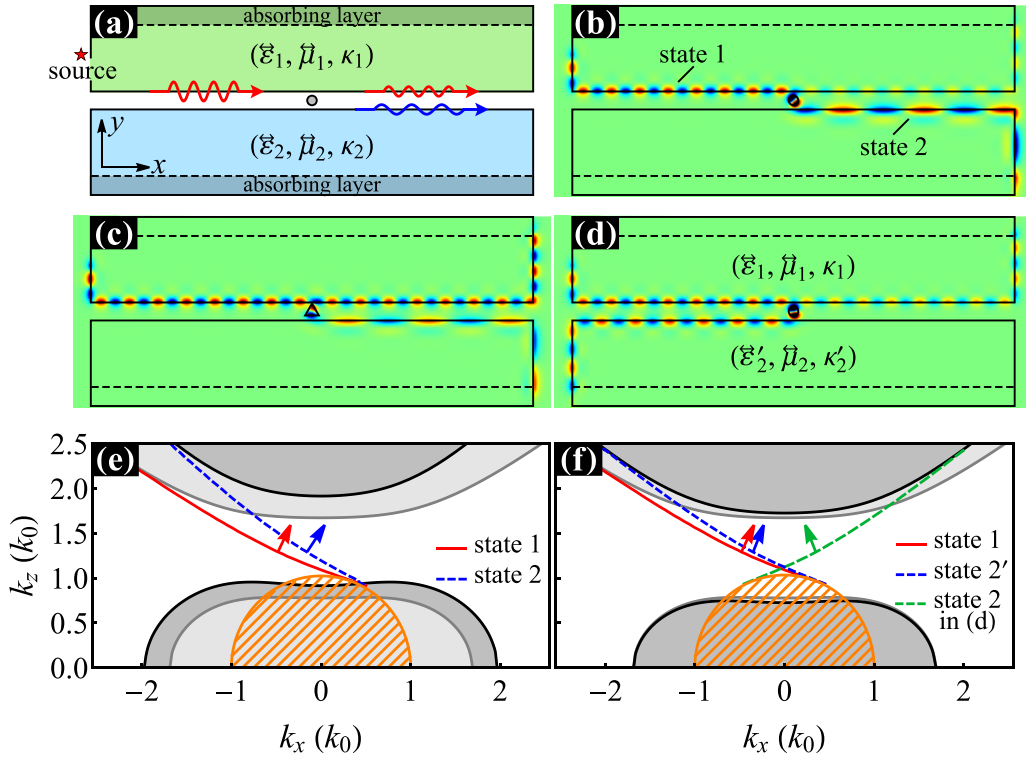


FIG. 2. (a) Configuration of the optical pulling system. (b)–(d) Surface waves scattered by particles inside the CHM waveguides. The constitutive parameters of the upper CHM are  $\vec{\epsilon}_1 = \text{diag}(3, 3, -4)$ ,  $\vec{\mu}_1 = \text{diag}(0.5, 0.5, 1)$ ,  $\kappa_1 = 0.45$ , and the relative permittivity of the dielectric particle in the air gap is  $\epsilon_r = 3$  in all cases. The constitutive parameters of the lower CHM are  $\vec{\epsilon}_2 = \text{diag}(4, 4, -3)$ ,  $\vec{\mu}_2 = \vec{\mu}_1$ ,  $\kappa_2 = -0.5$  in (b),(c) and  $\vec{\epsilon}'_2 = \text{diag}(3, 3, -3)$ ,  $\vec{\mu}_2 = \vec{\mu}_1$ ,  $\kappa_2 = -0.5$  in (d). (e),(f) Dispersion of the surface state 1 (red solid lines) and state 2 (blue dashed and green dashed lines). The arrows mark the directions of group velocities. The gray and orange shaded regions correspond to the bulk states of CHMs and the EFS of air, respectively. In (e), the upper and lower CHMs are the same as those used in (a)–(c). In (f), the upper CHM takes the same parameters as in (a)–(c), the lower CHM has the parameters  $(\vec{\epsilon}'_2, \vec{\mu}_2, \kappa_2)$  and  $(\vec{\epsilon}'_2, \vec{\mu}_2, \kappa'_2)$  for the blue dashed line and the green dashed line, respectively.

respectively. Due to TRS, the two intersections must have the same chirality, i.e.,  $\chi_{p+} = \chi_{p-} = -\text{sgn}(\kappa)$ . Therefore, the longitudinal (along the  $x$  direction) propagating directions of the surface-arc states are determined by the topological charge of the EFS. In what follows, we illustrate how to realize robust optical pulling using such chiral surface-arc states.

### III. ONE WAY TRANSPORTATION AND CONVERSION OF THE SURFACE-ARC WAVES

The configuration of the optical pulling system is schematically shown in Fig. 2(a), where an air gap is sandwiched between two lossless CHMs with different constitutive parameters  $(\vec{\epsilon}_1, \vec{\mu}_1, \kappa_1)$  and  $(\vec{\epsilon}_2, \vec{\mu}_2, \kappa_2)$ , respectively. A particle can move in the channel along the  $x$  direction, as indicated in Fig. 2(a). For the two parallel metamaterial surfaces facing the air gap, each one supports a topologically protected chiral surface-arc in the upper  $k_z$  gap between the bulk EFSs, and the corresponding surface-arc states propagate unidirectionally. In Fig. 2(e), the red solid (blue dashed) line depicts the surface-arc on the interface between the upper (lower) CHM and air, which we refer to as arc 1 (arc 2), and we call the surface states on the two arcs state 1 and state 2, respectively. A line source along the  $z$  axis, as marked by a red star in Fig. 2(a), is located near the left surface of the upper lossless

CHM to excite state 1. To prevent the surface waves from returning to the starting point after circling the CHMs, we attach an absorbing layer to each lossless CHM, as shown in Fig. 2(a). For the chosen  $k_z = 1.3k_0$ , where  $k_0$  is the wave number in vacuum, the longitudinal wave number  $k_{x2}$  of state 2 is less negative than  $k_{x1}$  of the state 1, which can be seen from Fig. 2(e). The group velocities of the surface states are normal to the corresponding surface arcs as marked by the arrows in Fig. 2(e). At  $k_z = 1.3k_0$ , both of the surface states propagate from left to right inside the air gap. Note that both  $k_{x1}$  and  $k_{x2}$  are negative, therefore the  $x$  components of the phase and group velocities of each state are in the opposite directions.

Consider a round particle located in the air gap. Since state 2 cannot be excited due to the mismatch of  $k_x$ , the incident surface wave will be confined on the surface of the upper CHM before being scattered by the particle, as shown by the full-wave simulation result in Fig. 2(b) obtained using the commercial package COMSOL. When the surface wave is scattered by the particle, plane-wave components of various  $k_x$  are generated around the particle (acting as a secondary line source), and state 2 is excited by the component with  $k_x = k_{x2}$ . Since only the two modes with  $k_x = k_{x1}$  and  $k_x = k_{x2}$  can propagate, all the optical energy will be distributed to the states 1 and 2. Due to the absence of a backward channel, the

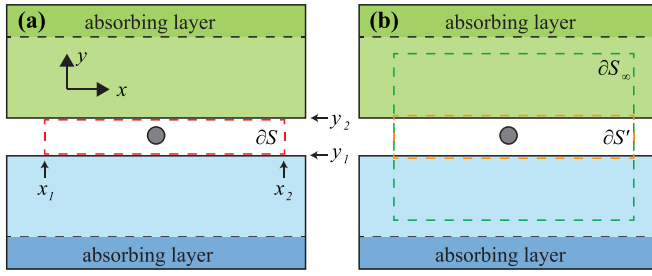


FIG. 3. Schematic of the closed surfaces for integrating the stress tensors. (a) The red dashed rectangle denotes the closed surface  $\partial S$  in the air. (b) The orange and green dashed rectangles are the closed surfaces  $\partial S'$  and  $\partial S_\infty$ , respectively.

incident wave cannot be reflected by the particle, independent of its material content, size, and shape. Therefore, even if we replace the round particle by a triangular one, the backward scattering is still totally suppressed, as shown in Fig. 2(c).

#### IV. THE LONGITUDINAL OPTICAL FORCE AND CONSERVATION OF THE MINKOWSKI-TYPE MOMENTA OF LIGHT

In this section, we will derive the optical force exerted by the surface-arc waves on a particle inside the air gap of the waveguide, and we will show that the optical force is rigorously proportional to the wave-number difference of the two surface-arc states. Since the particle is immersed in air, the optical force acting on the particle can be unambiguously evaluated by

$$\mathbf{F} = \oint_{\partial S} \overset{\leftrightarrow}{T}^{\max} \cdot \hat{n} dl, \quad (2)$$

where the time-averaged Maxwell stress tensor (MST) is expressed as

$$\overset{\leftrightarrow}{T}^{\max} = \frac{1}{2} \text{Re} [\varepsilon_0 \mathbf{E} \mathbf{E}^* + \mu_0 \mathbf{H} \mathbf{H}^* - \frac{1}{2} (\varepsilon_0 \mathbf{E} \cdot \mathbf{E}^* + \mu_0 \mathbf{H} \cdot \mathbf{H}^*) \mathbf{I}]. \quad (3)$$

$\partial S$  is an arbitrary closed surface that encloses the particle and is restricted in the region of the air gap, and  $\hat{n}$  is the outward normal unit vector of  $\partial S$ . Without loss of generality, we choose  $\partial S$  as a rectangle in the air waveguide with the upper (lower) horizontal boundary infinitely close to the lower (upper) surface of the waveguide from the side of air, as marked by the red dashed rectangle in Fig. 3(a). The  $x$  and  $y$  boundaries of the rectangle are at  $x_1, x_2$  and  $y_1, y_2$ , respectively. Then the longitudinal optical force (along the  $x$  direction) of the particle is calculated as

$$f_x = \int_{y_1}^{y_2} [T_{xx}^{\max}(x_2, y) - T_{xx}^{\max}(x_1, y)] dy + \int_{x_1}^{x_2} [T_{xy}^{\max}(x, y_2) - T_{xy}^{\max}(x, y_1)] dx. \quad (4)$$

In Eq. (4), we have the MST components  $T_{xx}^{\max} = \frac{1}{2} \text{Re} [E_x D_x^* + H_x B_x^* - \frac{1}{2} (\mathbf{E} \cdot \mathbf{D}^* + \mathbf{H} \cdot \mathbf{B}^*)]$  with  $\mathbf{D} = \varepsilon_0 \mathbf{E}$ ,  $\mathbf{B} = \mu_0 \mathbf{H}$  in air, and  $T_{xy}^{\max} = \frac{1}{2} \text{Re} (E_x D_y^* + H_x B_y^*)$ .

$T_{xy}^{\max}$  only depends on the field components  $E_x, D_y, H_x, B_y$  that are continuous across the boundaries of the CHMs. Therefore,  $T_{xy}^{\max}$  is continuous across the boundary, and the integration for the longitudinal optical force can be performed over  $\partial S'$ , whose upper (lower) boundary is infinitesimally close to the surface of the waveguide from the side of CHMs [see the dashed orange lines in Fig. 3(b)], and the integrand is then replaced by the time-averaged Minkowski stress tensor instead, namely

$$f_x = \hat{x} \cdot \oint_{\partial S'} \overset{\leftrightarrow}{T}^{\min} \cdot \hat{n} dl, \quad (5)$$

where the Minkowski stress tensor is expressed as

$$\overset{\leftrightarrow}{T}^{\min} = \frac{1}{2} \text{Re} [\mathbf{E} \mathbf{D}^* + \mathbf{H} \mathbf{B}^* - \frac{1}{2} (\mathbf{E} \cdot \mathbf{D}^* + \mathbf{H} \cdot \mathbf{B}^*) \mathbf{I}]. \quad (6)$$

We note that the above expression of the Minkowski stress tensor, as the spatial part of the electromagnetic energy-momentum tensor derived from Noether's theorem, is valid even in dispersive media [62,63]. Because the CHMs are homogeneous and lossless,  $\nabla \cdot \overset{\leftrightarrow}{T}^{\min} = 0$  is satisfied inside the CHMs [63] and hence the integral of the Minkowski stress tensor over any closed surface inside the material is always zero. Therefore,

$$f_x = \hat{x} \cdot \left[ \oint_{\partial S'} \overset{\leftrightarrow}{T}^{\min} \cdot \hat{n} dl + \oint_{\partial S_\infty - \partial S'} \overset{\leftrightarrow}{T}^{\min} \cdot \hat{n} dl \right] = \hat{x} \cdot \oint_{\partial S_\infty} \overset{\leftrightarrow}{T}^{\min} \cdot \hat{n} dl, \quad (7)$$

where  $\partial S_\infty$  is a very big rectangle with the upper and lower boundaries far away from the air waveguide; see the green dashed rectangle in Fig. 3(b). Since the electromagnetic fields decay away from the air waveguide, the electromagnetic fields vanish at the horizontal boundaries of the far side. So, we only need to consider the integration over the two vertical boundaries in Eq. (7), namely

$$f_x = \int_{-\infty}^{\infty} [T_{xx}^{\min}(x_2, y) - T_{xx}^{\min}(x_1, y)] dy. \quad (8)$$

Because the surface modes decay very fast away from the interfaces, the interference between the two surface modes can be safely neglected. So, we can calculate the contribution of each surface mode, respectively. For the incident state 1, the electromagnetic fields can be expressed as

$$(\mathbf{E}, \mathbf{H})^T = (e_x, e_y, e_z, h_x, h_y, h_z)^T e^{ik_x x + ik_z z}, \quad (9)$$

where  $e_i, h_i, i = x, y, z$  are  $y$ -dependent functions and vanish at infinity,  $y \rightarrow \pm\infty$ . According to Maxwell's equations,

$$\nabla \times \mathbf{E} = i\omega \mathbf{B}, \quad \nabla \times \mathbf{H} = -i\omega \mathbf{D}, \quad (10)$$

we obtain

$$\mathbf{D} = \frac{1}{\omega} (i\partial_y h_z + k_z h_y, k_{x1} h_z - k_z h_x, -k_{x1} h_y - i\partial_y h_x) e^{ik_x x + ik_z z},$$

$$\mathbf{B} = \frac{1}{\omega} (-i\partial_y e_z - k_z e_y, k_z e_x - k_{x1} e_z, k_{x1} e_y + i\partial_y e_x) e^{ik_x x + ik_z z}. \quad (11)$$

Substituting Eq. (9) into  $T_{xx}^{\min}$ , we obtain

$$\begin{aligned} T_{xx}^{\min} &= \frac{1}{2\omega} [\text{Re}(h_y^* e_z - h_z^* e_y) k_{x1} \\ &\quad - \text{Im}(e_z \partial_y h_z^* + h_z^* \partial_y e_x + e_z \partial_y h_x^* + h_x^* \partial_y e_z)] \\ &= \frac{1}{2\omega} \{\text{Re}(h_y^* e_z - h_z^* e_y) k_{x1} - \text{Im}[\partial_y(e_x h_z^* + e_z h_x^*)]\}. \end{aligned} \quad (12)$$

Then according to Eq. (8), the contribution of the incident state 1 to the longitudinal optical force is

$$\begin{aligned} & -\frac{k_{x1}}{2\omega} \text{Re} \int_{-\infty}^{\infty} (h_y^* e_z - h_z^* e_y) dy \\ & + \frac{1}{2\omega} \text{Im} \int_{-\infty}^{\infty} \partial_y (e_x h_z^* + e_z h_x^*) dy. \end{aligned} \quad (13)$$

The last integration of Eq. (13) vanishes since

$$\int_{-\infty}^{\infty} \partial_y (e_x h_z^* + e_z h_x^*) dy = (e_x h_z^* + e_z h_x^*)|_{-\infty}^{\infty} = 0 - 0 = 0, \quad (14)$$

and the first integration gives

$$-\frac{k_{x1}}{2\omega} \int_{-\infty}^{\infty} \text{Re}(h_y^* e_z - h_z^* e_y) dy = \frac{k_{x1}}{\omega} \langle S_{1x}^{\text{(inc)}} \rangle_{\text{tot}}, \quad (15)$$

where  $\langle S_{1x}^{\text{(inc)}} \rangle_{\text{tot}}$  is the total energy flux along the  $x$  direction of the incident state 1. Similarly, we can obtain the contributions from the scattered states 1 and 2. And the longitudinal optical force is then given by

$$f_x = \frac{k_{x1}}{\omega} (\langle S_{1x}^{\text{(inc)}} \rangle_{\text{tot}} - \langle S_{1x}^{\text{(sca)}} \rangle_{\text{tot}}) - \frac{k_{x2}}{\omega} |\langle S_{2x}^{\text{(sca)}} \rangle_{\text{tot}}|, \quad (16)$$

where  $\langle S_{1x}^{\text{(sca)}} \rangle_{\text{tot}}$  and  $\langle S_{2x}^{\text{(sca)}} \rangle_{\text{tot}}$  are the total energy fluxes along the  $x$  direction of the waves scattered to state 1 and state 2, respectively. Note that since state 1 is required to propagate rightward,  $\langle S_{1x}^{\text{(sca)}} \rangle_{\text{tot}}$  must take a positive value. In contrast,  $\langle S_{2x}^{\text{(sca)}} \rangle_{\text{tot}}$  can be either positive or negative. Nevertheless, as the directions of the energy fluxes of the scattered states are always parallel to the outward surface normal at the corresponding exit boundaries of  $\partial S_{\infty}$ , no matter whether the state 2 propagates leftward or rightward, the scattered wave in state 2 must offer a negative contribution to the total force, as expressed in Eq. (16). For the lossless case, the total energy flux should be conserved [64], which leads to

$$\langle S_{1x}^{\text{(inc)}} \rangle_{\text{tot}} - \langle S_{1x}^{\text{(sca)}} \rangle_{\text{tot}} = |\langle S_{2x}^{\text{(sca)}} \rangle_{\text{tot}}|. \quad (17)$$

From Eqs. (16) and (17), we obtain the explicit expression of the longitudinal optical force as

$$f_x = \frac{|\langle S_{2x}^{\text{(sca)}} \rangle_{\text{tot}}|}{\hbar\omega} \hbar(k_{x1} - k_{x2}). \quad (18)$$

The line density of the Minkowski momentum along the  $x$  direction  $g_x$  and the line energy density  $W$  is related by [58]

$$g_x = \frac{k_x}{\omega} W, \quad (19)$$

and the group velocity of a surface mode is defined as [58]

$$\mathbf{v}_g = \left( \int_{-\infty}^{\infty} \langle \mathbf{S} \rangle dy \right) / W, \quad (20)$$

where  $\langle \mathbf{S} \rangle$  is the Poynting vector of the surface wave. Substituting Eqs. (19) and (20) into Eq. (18), the longitudinal optical force can be further expressed as

$$f_x = v_{gx1} (g_{1x}^{\text{(inc)}} - g_{1x}^{\text{(sca)}}) - |v_{gx2}| g_{2x}^{\text{(sca)}}, \quad (21)$$

where  $v_{gx1}$ ,  $v_{gx2}$  are the group velocities along the  $x$  direction of the states 1 and 2, and  $g_{1x}^{\text{(inc)}}$ ,  $g_{1x}^{\text{(sca)}}$ ,  $g_{2x}^{\text{(sca)}}$  are the Minkowski momentum line densities of the incident state 1, scattered state 1, and scattered state 2, respectively. From the microscopic perspective, the Minkowski momentum and energy of a single photon are  $\hbar\omega$  and  $\hbar\mathbf{k}$ . Using the line number density of photons  $N = W/(\hbar\omega) = g_x/(\hbar k_x)$ , Eq. (21) can be written as

$$f_x = (N_1^{\text{(inc)}} - N_1^{\text{(sca)}}) v_{gx1} \hbar k_{x1} - N_2^{\text{(sca)}} |v_{gx2}| \hbar k_{x2}, \quad (22)$$

where  $N_1^{\text{(inc)}}$ ,  $N_1^{\text{(sca)}}$ ,  $N_2^{\text{(sca)}}$  are the line number densities of the photons of the incident state 1, scattered state 1, and scattered state 2, respectively. Equation (22) indicates that the longitudinal optical force is equal to the change of total Minkowski momentum of light per unit time, consistent with the law of linear momentum conservation. Note that  $N_1^{\text{(inc)}} v_{gx1} \hbar\omega$ ,  $N_1^{\text{(sca)}} v_{gx1} \hbar\omega$ ,  $N_2^{\text{(sca)}} v_{gx2} \hbar\omega$  are the total energy fluxes of the incident state 1, scattered state 1, and scattered state 2, respectively, so Eqs. (22) and (18) are equivalent.

Equation (18) shows that the longitudinal optical force on the particle is proportional to the wave-number difference between the incident and the scattered surface states,  $(k_{x1} - k_{x2})$ . Since the linear Minkowski momentum of a surface mode supported by a homogeneous medium is proportional to  $\mathbf{k}$  [58], we can conclude that the longitudinal optical force is entirely converted from the Minkowski momenta of the surface modes [59]. Interestingly, the surface states 1 and 2 have backward Minkowski momentum while they propagate forward along the  $x$  direction.

It is worthwhile to remark that despite the long debate on the definition of the momentum of light in media, known as the Minkowski-Abraham controversy [65], our derivation does not rely on a special choice or definition of optical momentum, because the particle is placed in air, where all variants of stress tensors of electromagnetic fields are reduced to the Maxwell stress tensor. As a result, the derived optical force is not complicated by the Minkowski-Abraham controversy, which in turn demonstrates that the Minkowski momentum of surface waves plays a practical role in light-matter interaction.

## V. OPTICAL PULLING

Since  $f_x$  is proportional to  $k_{x1} - k_{x2}$  and  $k_{x1} < k_{x2}$ ,  $f_x$  is always negative, as long as a part of the incident wave of state 1 is transferred into state 2 with a less negative  $k_x$  incurred by the scattering. Therefore, the optical pulling is robust irrespective of the particle's material, size, and shape. These parameters only affect the conversion efficiency from state 1 to state 2 and hence the magnitude of the pulling force.

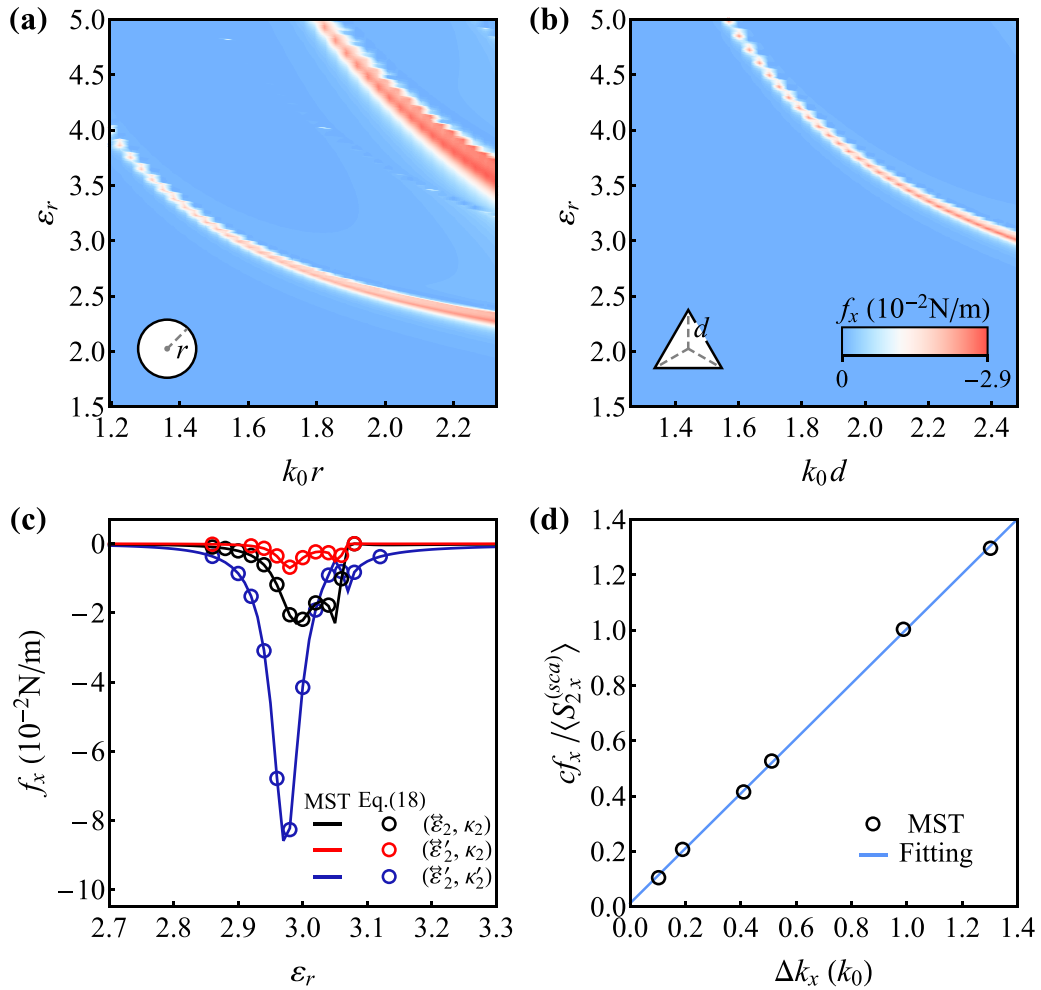


FIG. 4. The longitudinal optical force as a function of the dimensionless size parameter (a)  $k_0 r$  and (b)  $k_0 d$  and the relative permittivity of the (a) round and (b) triangular particle. The unit of force is N/m, and the amplitude of the source current is 1 A. The out-of-plane wave number is  $k_z = 1.3k_0$ . (c)  $f_x$  on the round particle ( $k_0 r = 0.5\pi$ ) as functions of the particle' relative permittivity  $\epsilon_r$  for three different lower CHMs with the parameters  $(\vec{\epsilon}'_2, \vec{\mu}_2, \kappa_2)$ (black),  $(\vec{\epsilon}'_2, \vec{\mu}_2, \kappa_2)$ (red), and  $(\vec{\epsilon}'_2, \vec{\mu}_2, \kappa'_2)$  (blue), respectively. The lines and circles denote the results using the MST and Eq. (18). (d) Linear fitting of  $\langle c f_x \rangle / \langle S_{2x}^{(sca)} \rangle_{\text{tot}}$  (light-blue line) as a function of  $\Delta k_x = k_{x2} - k_{x1}$ .

In Figs. 4(a) and 4(b), the longitudinal optical forces calculated using MST on (a) a round and (b) a triangular dielectric particle located in the air gap changing with their relative permittivities and size are displayed, which shows that  $f_x$  is always negative. The strong optical pulling force denoted by the red regions is attributed to the multipolar resonances of the particles where the scattering is enhanced. Although the pulling force can be amplified by the multipolar resonances, we stress that the pulling nature does not rely on these details, which is in sharp contrast with the ordinary pulling scheme using structured beams where optical pulling can only be realized via simultaneous excitation of multiple multipolar resonances of the particle [3].

The strength of the pulling force can be tuned by controlling the wave-number difference  $\Delta k_x = k_{x2} - k_{x1}$  according to Eq. (18). In Fig. 4(c), we show the longitudinal optical forces on a round particle calculated using MST (plotted by lines) for three different CHM waveguides, and we compare the results with those obtained by Eq. (18) (plotted by cir-

cles). The first CHM waveguide (data in black) corresponds to Fig. 2(b). In the second scenario (red), by changing the relative permittivity tensor of the lower CHM to  $\vec{\epsilon}'_2$ , the value of  $\Delta k_x$  is reduced [the momentum gap between the red solid and blue dashed lines in Fig. 2(f) is smaller than that in Fig. 2(e)]. Consequently, the pulling force is significantly smaller than that in the first case. In the third case (blue), we further change the sign of the chiral coupling to  $\kappa'_2 = -\kappa_2$ ; the chirality of the surface arc 2 [green dashed line in Fig. 2(f)] is reversed accordingly. Although light is reflected by the particle in this case [see the full-wave simulation in Fig. 2(d)], we found the counterintuitive fact that the optical force is still pulling and remarkably larger than the other two cases, since the positive longitudinal wave number  $k_{x2}$  of state 2 leads to a larger  $\Delta k_x$ . For all three cases, the results by MST and Eq. (18) agree perfectly with each other; see Fig. 2(c). In Fig. 2(d). We further demonstrate that the numerically calculated optical forces normalized by the scattered energy fluxes,  $\langle c f_x \rangle / \langle S_{2x}^{(sca)} \rangle_{\text{tot}}$ , exhibit a strict linear dependence on  $\Delta k_x$  regardless of the parameters of the particle and the CHMs,

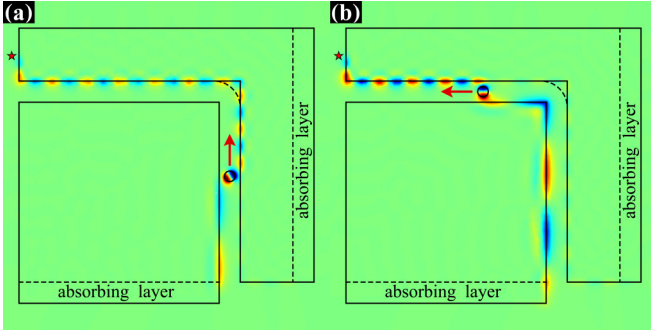


FIG. 5. The profile of surface waves inside the air waveguide with a  $90^\circ$  bend. The dashed arc denotes a thin and transparent barrier. The arrows show the optical force directions.

thereby substantiating the theory. Although Eq. (18) is derived by assuming that the CHMs are homogeneous and lossless, the optical pulling scheme still works even when the CHMs are lossy and subjected to a modest material imperfection, because the topological properties of the CHMs remain invariant under such conditions; see the details in the Supplemental Material [60], Sec. 3.

## VI. MOTIONS OF PARTICLES PASSING THROUGH THE BENDS

Because the CHMs are isotropic in the  $xy$  plane, the chiral surface arcs on any truncated surface parallel to the  $z$  axis have the same dispersion, and the surface waves can travel around corners without any reflection. Thus, a particle can be pulled continuously in a curved air gap.

As a typical example, we consider that the air waveguide has a  $90^\circ$  bend, as shown in Fig. 5. The particle is first subjected to an upward optical force in the vertical region until reaching the corner region [see Fig. 5(a)], and then it moves into the horizontal region directly or after elastic collisions with the modified corner boundaries. After that, it will be pulled towards the left end [see Fig. 5(b)].

To investigate how the particle passes through the bend when it is initially placed near the corner with zero velocity, we calculated the optical forces  $\mathbf{F}$  as well as the curl of the optical forces  $\nabla \times \mathbf{F} \cdot \hat{z}$  acting on the particle when it is located inside the corner region in Fig. 5, and we showed the results in Figs. 6(a) and 6(b), respectively. We ensure that the particle's mass center cannot reach the white regions in Figs. 6(a) and 6(b) by introducing an arc-shaped barrier at the corner (the dashed arc in Fig. 5). As shown in Fig. 6(a), the optical

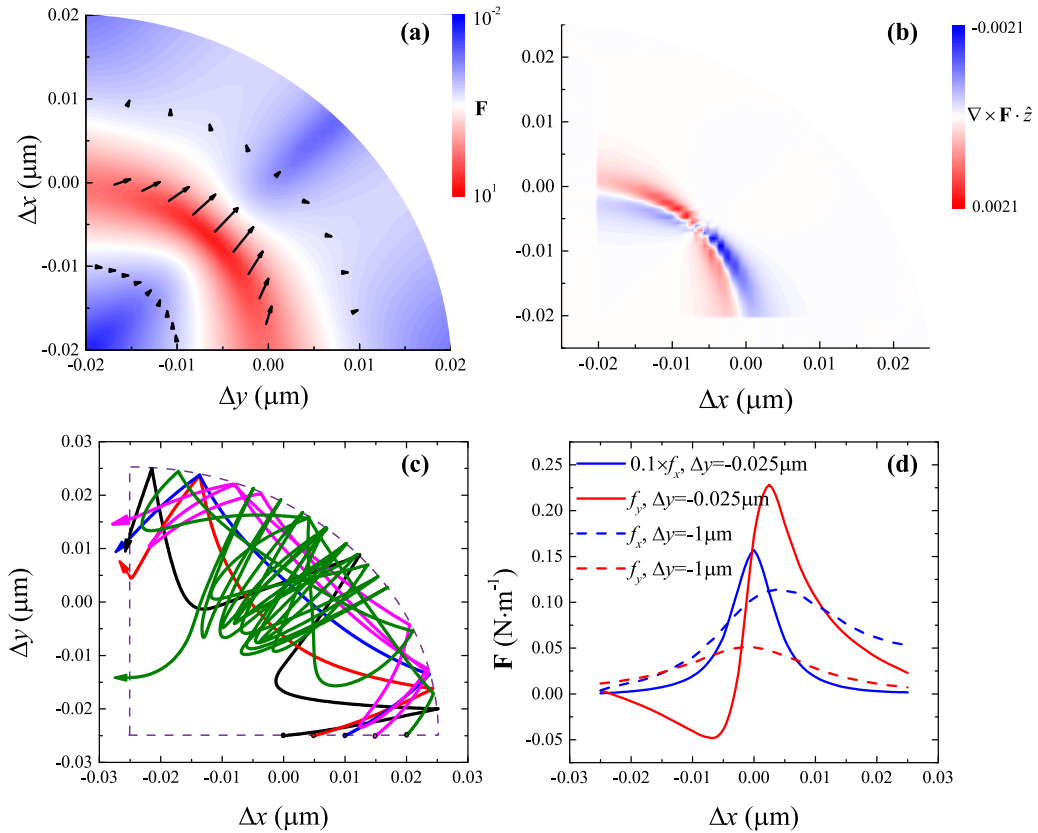


FIG. 6. Force and movement of the particle inside the corner region shown in Fig. 5. (a) The optical force amplitude  $|\mathbf{F}|$  (N/m) and (b) the curl of the optical force along the  $z$  direction  $\nabla \times \mathbf{F} \cdot \hat{z}$  ( $\text{N}/\mu\text{m}^2$ ) as functions of the particle's location. The center of the corner region is at  $\Delta x = \Delta y = 0$ . The arrows in (a) show the directions of the optical force. (c) Trajectories of the mass center of the particle when it passes through the corner region. The particle starts to move at different horizontal positions with zero initial velocity. The purple dashed line outlines the shape of the corner region. The radius and mass density of the particle are  $r = 0.5\pi/k_0$  and  $1050 \text{ kg/m}^3$ , respectively. (d) The  $x$  and  $y$  components of the optical forces acting on the particles located at the lower boundary of the corner region (solid lines) and away from the corner region (dashed lines).

forces mainly point towards the top right vertex of the corner region, indicating that there is a trapping potential for the particle inside the corner. However, the nonzero  $\nabla \times \mathbf{F} \cdot \hat{\mathbf{z}}$  indicates that the particle will undergo a nonconservative optical scattering force [66,67] and gain energy when it moves around inside the corner region. Therefore, even if the particle has no kinetic energy when it is entering the corner region, it can be accelerated by the nonconservative optical force and eventually escape from the corner region. In Fig. 6(c), we show the trajectories of a particle started at different points, labeled by the coordinate  $\Delta x$ , on the lower boundary of the corner region with zero velocity. The trajectories are calculated based on the motion equation of the particle  $m\dot{\mathbf{r}} = \mathbf{F}(\mathbf{r})$ , where  $\mathbf{F}(\mathbf{r})$  is the optical force,  $m$  is the mass of the particle, and the damping of air is ignored. We suppose that perfectly elastic collision occurs when the particle hits the arc-shaped barrier and the boundaries of the waveguide. The horizontal coordinates of the starting positions are all non-negative ( $\Delta x \geq 0$ ). We can see that the particle can escape from the corner region and move into the horizontal region of the waveguide for all starting positions. For the case of negative starting positions  $\Delta x < 0$  and zero initial velocity, the particle will be subject to an optical force along the negative- $y$  direction at first, see the red solid line in Fig. 6(d), and thus be pushed away from the corner region. However, after the particle leaves the corner region and moves into the vertical region ( $\Delta y < 0$ ), it will be accelerated along the  $+y$  direction by the optical pulling force, see the red dashed line in Fig. 6(d), and be attracted to  $\Delta x \geq 0$  due to the gradient force along the  $x$  direction [see the blue lines in Fig. 6(d)]. Therefore, the particle at starting positions  $\Delta x < 0$  will reenter the corner region of  $\Delta x \geq 0$  carrying a kinetic energy. Then it can pass through the corner region by overcoming the trapping potential and move into the horizontal region of the waveguide. In the Supplemental Material [60], Sec. 4, we further show that the particle can also be pulled passing through a  $60^\circ$  bend. All these results suggest

that the particle can be pulled along a complex trajectory confined by a meandering waveguide.

## VII. CONCLUSION

In summary, we proposed a scheme to realize robust and long-range optical pulling using two topologically protected chiral surface arcs on two facing CHMs. Based on a rigorous derivation using the electromagnetic energy-momentum tensor, we proved that the longitudinal optical force on the particle immersed in the air waveguide sandwiched by the two CHMs is entirely converted from the Minkowski momenta of the surface modes and is just proportional to the wave-number difference between the incident and scattered surface-arc modes. Therefore, we can realize robust optical pulling or switch it to optical pushing by simply selecting the launched state, irrespective of the particle's material, size, and shape. The advantage of employing a metamaterial is its homogeneity in the long-wavelength limit. Benefiting from the isotropy of the metamaterial in the  $xy$  plane, we can pull the particle along an arbitrary 2D trajectory by designing the shape of the surface-wave waveguide. With the advance in nanoengineering technology for realizing hyperbolic and chiral metamaterials at the working wavelengths of optical forces [61,68], our robust optical pulling scheme can provide an additional tool for the optical micromanipulations of matter.

## ACKNOWLEDGMENTS

We thank Xiaohan Cui for the help in the numerical simulations. This work is supported by National Natural Science Foundation of China (NSFC) through Grants No. 11904237 and No. 12174263, and the Research Grants Council of the Hong Kong Special Administrative Region through Grants No. AoE/P-02/12, No. 16303119, and CityU 11306019.

- 
- [1] S. Sukhov and A. Dogariu, *Opt. Lett.* **35**, 3847 (2010).
  - [2] S. Sukhov and A. Dogariu, *Phys. Rev. Lett.* **107**, 203602 (2011).
  - [3] J. Chen, J. Ng, Z. F. Lin, and C. T. Chan, *Nat. Photon.* **5**, 531 (2011).
  - [4] J. Saenz, *Nat. Photon.* **5**, 514 (2011).
  - [5] A. Novitsky, C. W. Qiu, and H. Wang, *Phys. Rev. Lett.* **107**, 203601 (2011).
  - [6] A. Novitsky, C.-W. Qiu, and A. Lavinenko, *Phys. Rev. Lett.* **109**, 023902 (2012).
  - [7] O. Brzobohaty, V. Karasek1, M. Siler1, L. Chvatal, T. Cizmar, and P. Zemanek, *Nat. Photon.* **7**, 123 (2013).
  - [8] X. Li, J. Chen, Z. Lin, and J. Ng, *Sci. Adv.* **5**, eaau7814 (2019).
  - [9] D. B. Ruffner and D. G. Grier, *Phys. Rev. Lett.* **109**, 163903 (2012).
  - [10] N. Wang, J. Chen, S. Liu, and Z. Lin, *Phys. Rev. A* **87**, 063812 (2013).
  - [11] N. Wang, W. Lu, J. Ng, and Z. Lin, *Opt. Lett.* **39**, 2399 (2014).
  - [12] A. V. Maslov, *Phys. Rev. Lett.* **112**, 113903 (2014).
  - [13] N. K. Paul and B. A. Kemp, *Prog. Electromagn. Res.* **151**, 73 (2015).
  - [14] N. K. Paul and B. A. Kemp, *Opt. Eng.* **55**, 015106 (2016).
  - [15] T. Zhu, M. R. Mahdy, Y. Cao, H. Lv, F. Sun, Z. Jiang, and W. Ding, *Opt. Express* **24**, 18436 (2016).
  - [16] T. Zhang, S. Mei, Q. Wang, H. Liu, C. T. Lim, and J. Ten, *Nanoscale* **9**, 6895 (2017).
  - [17] T. Zhu, A. Novitsky, Y. Cao, M. R. C. Mahdy, L. Wang, F. Sun, Z. Jiang, and W. Ding, *Appl. Phys. Lett.* **111**, 061105 (2017).
  - [18] T. Zhu, Y. Cao, L. Wang, Z. Nie, T. Cao, F. Sun, Z. Jiang, M. Nieto-Vesperinas, Y. Liu, C.-W. Qiu, and W. Ding, *Phys. Rev. Lett.* **120**, 123901 (2018).
  - [19] H. Li, Y. Cao, B. Shi, T. Zhu, Y. Geng, R. Feng, L. Wang, F. Sun, Y. Shi, M. A. Miri, M. Nieto-Vesperinas, C.-W. Qiu, and W. Ding, *Phys. Rev. Lett.* **124**, 143901 (2020).
  - [20] D. Wang and Z. Wang, in *Proceedings of the 2017 Conference on Lasers and Electro-Optics, Singapore*, p. FTh1H.4 (IEEE, 2017).
  - [21] S. Wang, J. Ng, M. Xiao, and C. T. Chan, *Sci. Adv.* **2**, e1501485 (2016).
  - [22] A. S. Shalin, S. V. Sukhov, A. A. Bogdanov, P. A. Belov, and P. Ginzburg, *Phys. Rev. A* **91**, 063830 (2015).

- [23] F. D. M. Haldane and S. Raghu, *Phys. Rev. Lett.* **100**, 013904 (2008).
- [24] S. Raghu and F. D. M. Haldane, *Phys. Rev. A* **78**, 033834 (2008).
- [25] Z. Wang, Y. D. Chong, J. D. Joannopoulos, and M. Soljacic, *Phys. Rev. Lett.* **100**, 013905 (2008).
- [26] Z. Wang, Y. Chong, J. D. Joannopoulos, and M. Soljacic, *Nature (London)* **461**, 772 (2009).
- [27] L. Lu, J. D. Joannopoulos, and M. Soljacic, *Nat. Photon.* **8**, 821 (2014).
- [28] M. Xiao, Z.-Q. Zhang, and C. T. Chan, *Phys. Rev. X* **4**, 021017 (2014).
- [29] A. B. Khanikaev, S. H. Mousavi, W.-K. Tse, M. Kargarian, A. H. MacDonald, and G. Shvets, *Nat. Mater.* **12**, 233 (2013).
- [30] L.-H. Wu and X. Hu, *Phys. Rev. Lett.* **114**, 223901 (2015).
- [31] L. Lu, J. D. Joannopoulos, and M. Soljacic, *Nat. Phys.* **12**, 626 (2016).
- [32] S. A. Skirlo, L. Lu, and M. Soljacic, *Phys. Rev. Lett.* **113**, 113904 (2014).
- [33] T. Ma and G. Shvets, *New. J. Phys.* **18**, 025012 (2016).
- [34] M. Xiao and S. Fan, *Phys. Rev. B* **96**, 100202(R) (2017).
- [35] Y. Poo, R.-X. Wu, Z. Lin, Y. Yang, and C. T. Chan, *Phys. Rev. Lett.* **106**, 093903 (2011).
- [36] D. Wang, C.-W. Qiu, P. T. Rakich, and Z. Wang, in *CLEO: QELS Fundamental Science* (Optical Society of America, 2015).
- [37] W. Gao, M. Lawrence, B. Yang, F. Liu, F. Fang, B. Beri, J. Li, and S. Zhang, *Phys. Rev. Lett.* **114**, 037402 (2015).
- [38] B. Yang, Q. Guo, B. Tremain, L. E. Barr, W. Gao, H. Liu, B. Beri, Y. Xiang, D. Fan, A. P. Hibbins, and S. Zhang, *Nat. Commun.* **8**, 7 (2017).
- [39] X. Wan, A. M. Turner, A. Vishwanath, and S. Y. Savrasov, *Phys. Rev. B* **83**, 205101 (2011).
- [40] S.-Y. Xu, I. Belopolski, N. Alidoust, M. Neupane, G. Bian *et al.*, *Science* **349**, 613 (2015).
- [41] B. Q. Lv, H. M. Weng, B. B. Fu, X. P. Wang, H. Miao, J. Ma, P. Richard, X. C. Huang, L. X. Zhao, G. F. Chen, Z. Fang, X. Dai, T. Qian, and H. Ding, *Phys. Rev. X* **5**, 031013 (2015).
- [42] B. Q. Lv, N. Xu, H. M. Weng, J. Z. Ma, P. Richard *et al.*, *Nat. Phys.* **11**, 724 (2015).
- [43] S.-Y. Xu, N. Alidoust, I. Belopolski, Z. Yuan, G. Bian *et al.*, *Nat. Phys.* **11**, 748 (2015).
- [44] F. D. M. Haldane, [arXiv:1401.0529](https://arxiv.org/abs/1401.0529).
- [45] I. Belopolski, S.-Y. Xu, D. S. Sanchez, G. Chang, C. Guo, M. Neupane *et al.*, *Phys. Rev. Lett.* **116**, 066802 (2016).
- [46] N. P. Armitage, E. J. Mele, and A. Vishwanath, *Rev. Mod. Phys.* **90**, 015001 (2018).
- [47] L. Lu, L. Fu, J. D. Joannopoulos, and M. Soljacic, *Nat. Photon.* **7**, 294 (2013).
- [48] L. Lu, Z. Wang, D. Ye, L. Ran, L. Fu, J. D. Joannopoulos, and M. Soljacic, *Science* **349**, 622 (2015).
- [49] M. Xiao, W.-J. Chen, W.-Y. He, and C. T. Chan, *Nat. Phys.* **11**, 920 (2015).
- [50] M. Xiao, Q. Lin, and S. Fan, *Phys. Rev. Lett.* **117**, 057401 (2016).
- [51] W. Gao, B. Yang, M. Lawrence, F. Fang, B. Beri, and S. Zhang, *Nat. Commun.* **7**, 12435 (2016).
- [52] W.-J. Chen, M. Xiao, and C. T. Chan, *Nat. Commun.* **7**, 13038 (2016).
- [53] B. Yang, Q. Guo, B. Tremain, R. Liu, L. E. Barr *et al.*, *Science* **359**, 1013 (2018).
- [54] M.-L. Chang, M. Xiao, W.-J. Chen, and C. T. Chan, *Phys. Rev. B* **95**, 125136 (2017).
- [55] J. Noh, S. Huang, D. Leykam, Y. D. Chong, K. P. Chen, and M. C. Rechtsman, *Nat. Phys.* **13**, 611 (2017).
- [56] H. He, C. Qiu, L. Ye, X. Cai, X. Fan, M. Ke, F. Zhang, and Z. Liu, *Nature (London)* **560**, 61 (2018).
- [57] H. Jia, W. Gao, Y. Xiang, H. Liu, and S. Zhang, *Ann. Phys. (Berlin)* **530**, 1800118 (2018).
- [58] K. Y. Bliokh, A. Y. Bekshaev, and F. Nori, *Phys. Rev. Lett.* **119**, 073901 (2017).
- [59] N. Wang, R.-Y. Zhang, S. Wang, G. P. Wang, and C. T. Chan, *Opt. Express* **29**, 20590 (2021).
- [60] See Supplemental Material at <http://link.aps.org/supplemental/10.1103/PhysRevB.105.014104> which includes Refs. [69,70], for details about the microscopic model and metallic helical structural design of the chiral hyperbolic media, the effects of the loss and material imperfections, and the motions of particles passing through the 60° bend.
- [61] P. Shekhar, J. Atkinson, and Z. Jacob, *Nano Converg.* **1**, 14 (2014).
- [62] T. G. Philbin, *Phys. Rev. A* **83**, 013823 (2011).
- [63] R.-Y. Zhang, Z. Xiong, N. Wang, Y. Chen, and C. T. Chan, *J. Opt. Soc. Am. B* **38**, 3135 (2021).
- [64] J. D. Jackson, *Classical Electrodynamics* (Wiley, New York, 1999).
- [65] R. N. C. Pfeifer, T. A. Nieminen, N. R. Heckenberg, and H. Rubinsztein-Dunlop, *Rev. Mod. Phys.* **79**, 1197 (2007).
- [66] J. Du, C.-H. Yuen, X. Li, K. Ding, G. Du, Z. Lin, C. T. Chan, and J. Ng, *Sci. Rep.* **7**, 18042 (2017).
- [67] N. Wang, X. Li, J. Chen, Z. Lin, and J. Ng, *Sci. Rep.* **8**, 17423 (2018).
- [68] M. Hentschel, M. Schäferling, X. Duan, H. Giessen, and N. Liu, *Sci. Adv.* **3**, e1602735 (2017).
- [69] R. Zhao, T. Koschny, and C. M. Soukoulis, *Opt. Express* **18**, 14553 (2010).
- [70] C. Liu, W. Gao, B. Yang, and S. Zhang, *Phys. Rev. Lett.* **119**, 183901 (2017).